



Cite this: *RSC Adv.*, 2025, **15**, 22930

## Comparative study of monoclinic and cubic $\text{WO}_3$ nanoplates on $\text{NO}_2$ gas-sensing properties†

Dang Trung Do, <sup>\*a</sup> Do Y Nhi Nguyen, <sup>b</sup> Thi Anh Pham, <sup>b</sup> Cong Tu Nguyen <sup>\*b</sup> and Van Hieu Nguyen <sup>c</sup>

Monoclinic and cubic  $\text{WO}_3$  nanoplates were controllably prepared from orthorhombic  $\text{WO}_3 \cdot \text{H}_2\text{O}$  ( $\text{o-WO}_3 \cdot \text{H}_2\text{O}$ ) nanoplates via a facile calcination method at 200 °C for 2 hours in ambient air using tubular and muffle furnaces, respectively. The  $\text{o-WO}_3 \cdot \text{H}_2\text{O}$  nanoplates were previously prepared from  $\text{Na}_2\text{WO}_4 \cdot 2\text{H}_2\text{O}$  via an acid precipitation method at room temperature. Calcination stimulated the dehydration and phase transformation from hydrated  $\text{WO}_3 \cdot \text{H}_2\text{O}$  nanoplates to  $\text{WO}_3$  nanoplates, and different crystal structures were observed under different air environments. In an open-air environment (tubular furnace), a stable monoclinic  $\text{WO}_3$  ( $\text{m-WO}_3$ ) phase was obtained, while in a closed-air environment (muffle furnace), a high-entropy cubic  $\text{WO}_3$  ( $\text{c-WO}_3$ ) phase was obtained. The difference in the phase transformation was confirmed using various physicochemical analyses, such as X-ray diffraction, field emission scanning electron microscopy, Brunauer–Emmett–Teller measurement, diffuse reflectance spectroscopy, and Raman scattering spectroscopy. Both  $\text{m-WO}_3$  and  $\text{c-WO}_3$  exhibited excellent  $\text{NO}_2$  gas-sensing performance, with ultra-high sensitivity, exceptional selectivity, and ultra-low theoretical limit of detection, at a mild optimal-working temperature of 150 °C. In particular, chemiresistive sensors based on  $\text{m-WO}_3$  and  $\text{c-WO}_3$  nanomaterials exhibited responses of 1322 and 780 to 2.5 ppm  $\text{NO}_2$  and theoretical limits of detection of 0.10 and 0.05 ppb to  $\text{NO}_2$  at 150 °C, respectively. These results imply that the phase transformation of  $\text{WO}_3$  nanostructures or even phase junctions could be achieved via a facile calcination process in different controlled environments (in closed or open ambient air) for various designed applications such as gas sensors.

Received 14th March 2025

Accepted 19th June 2025

DOI: 10.1039/d5ra01820j

rsc.li/rsc-advances

### 1. Introduction

Recently, air pollution has emerged as a significant global concern, especially in developing countries. Air pollution is mainly attributed to the presence of toxic gases, including  $\text{NH}_3$ ,  $\text{NO}_2$ ,  $\text{H}_2\text{S}$ ,  $\text{CO}$ , and volatile organic chemicals, which are mostly emitted as a result of various human activities.<sup>1,2</sup> Among these gases,  $\text{NO}_2$  is one of the most active candidates affecting human health. Hence, advancing the research and development of sensors for detecting low concentrations of these gases is of practical importance for monitoring toxic gas emissions and other related applications.

Various metal oxide semiconductor (MOS) nanomaterials, such as  $\text{SnO}_2$ ,  $\text{ZnO}$ ,  $\text{TiO}_2$ ,  $\text{In}_2\text{O}_3$  and  $\text{WO}_3$ , have been developed and extensively studied as gas-sensing materials, demonstrating promising applications in gas sensors.<sup>3–7</sup> Among these

MOS nanomaterials, tungsten trioxide ( $\text{WO}_3$ ) is one of the most promising candidates for detecting toxic gases owing to its abundance and excellent chemical stability and electrical conductivity.<sup>8</sup> Tungsten oxide also has high sensitivity to gases including  $\text{NO}_2$ ,  $\text{H}_2$ ,  $\text{H}_2\text{S}$ ,  $\text{NH}_3$ , and  $\text{CO}$ .<sup>9–13</sup> Notably,  $\text{WO}_3$  exhibits outstanding selectivity for  $\text{NO}_2$  detection.<sup>14–17</sup> To date, different  $\text{WO}_3$  nanostructures, such as nanobelts, nanowires, nanoflakes, nanosheets, and nanofibers, have been fabricated using several methods. Each morphology exhibits good gas-sensing properties for specific target gases.<sup>18–22</sup>

The crystal phase of  $\text{WO}_3$  nanomaterials is a key factor influencing the gas-sensing performance of the sensor. Different phases of  $\text{WO}_3$  nanostructures, such as monoclinic, orthorhombic, hexagonal ( $\text{h-WO}_3$ ), triclinic, and mixed phases, have been reported recently.<sup>23–28</sup> During the synthesis process, various factors, such as the dosing ratio, reaction temperature, reaction duration, and calcination temperature, can influence the crystalline phase, grain size, and crystal morphology, thereby affecting the gas-sensing performance. Liu and coworkers prepared orthorhombic  $\text{WO}_3$  ( $\text{o-WO}_3$ ) nanorods and  $\text{m-WO}_3$  via a facile hydrothermal synthesis at 180 °C. Results revealed that the  $\text{m-WO}_3$ -based sensor exhibited a remarkably better response to  $\text{NO}_2$  than the  $\text{o-WO}_3$ -based sensor.<sup>29</sup> Chen

<sup>a</sup>Department of Fundamental of Fire Fighting and Prevention, University of Fire Fighting and Prevention, Hanoi, Vietnam. E-mail: trungdo81@gmail.com

<sup>b</sup>Faculty of Engineering Physics, Hanoi University of Science and Technology, Hanoi, Vietnam. E-mail: tu.nguyencong@hust.edu.vn

<sup>c</sup>Faculty of Electrical and Electronic Engineering, Phenikaa University, Hanoi, Vietnam

† Electronic supplementary information (ESI) available. See DOI: <https://doi.org/10.1039/d5ra01820j>



and coworkers prepared and compared the gas sensing performance of o-WO<sub>3</sub> and m-WO<sub>3</sub> nanosheets, which were synthesized by adjusting the synthesis temperature.<sup>30</sup> o-WO<sub>3</sub> nanosheets were formed at temperature below 150 °C, while the transition from orthorhombic to monoclinic occurred at a higher synthesis temperature of 180 °C. The results showed that the m-WO<sub>3</sub> nanosheets exhibited better gas sensitivity than the o-WO<sub>3</sub> nanosheets. L. Zhang and coworkers investigated the gas sensing performance of o-WO<sub>3</sub> and c/o-WO<sub>3</sub> through a one-step calcination process at temperatures ranging from 500 °C to 1000 °C. The c/o-WO<sub>3</sub> sample, calcined at 800 °C, demonstrated a response value of 5.23 to 0.5 ppm of NO<sub>2</sub> and exhibited high selectivity, excellent stability, and reliable repeatability.<sup>31</sup> S. Wei *et al.* fabricated h-WO<sub>3</sub> and o-WO<sub>3</sub> *via* a hydrothermal technique and compared their CO gas-sensing performances. Their findings revealed that variations in the morphology and crystal phase played key roles in the gas-sensing property. The h-WO<sub>3</sub> sensor demonstrated outstanding CO sensing performance at 270 °C and provided a quicker and more enhanced response than that of the o-WO<sub>3</sub> sensor.<sup>27</sup>

Numerous studies have been published on the gas sensing performances of various crystal phases of WO<sub>3</sub> nanostructures. However, up to now, there have been very few reports on comparative studies of the effects of monoclinic and cubic WO<sub>3</sub> nanostructures on NO<sub>2</sub> gas-sensing applications. In this work, monoclinic and cubic WO<sub>3</sub> nanoplates were selectively synthesized from WO<sub>3</sub>·H<sub>2</sub>O nanoplates *via* a facile calcination process in regulated environments using different furnaces. Initially, WO<sub>3</sub>·H<sub>2</sub>O nanoplates were prepared *via* a facile and power-saving acid precipitation method at room temperature (RT). The effects of the calcination condition on the morphology and crystal structure of samples were investigated using field emission scanning electron microscopy, X-ray diffraction, Brunauer-Emmett-Teller analysis, and diffuse reflectance

spectroscopy. The NO<sub>2</sub> gas sensing performance of the sensors were tested using a chemiresistive configuration. Results revealed that both the monoclinic and cubic WO<sub>3</sub> nanoplates exhibited excellent NO<sub>2</sub> gas-sensing characteristics, in which monoclinic WO<sub>3</sub> nanoplates exhibited a better response than those of cubic WO<sub>3</sub> nanoplates. The gas-sensing mechanism and the difference in gas sensing performance of m-WO<sub>3</sub> and c-WO<sub>3</sub>-based gas sensors were also discussed.

## 2. Experimental

### 2.1. Synthesis of monoclinic and cubic WO<sub>3</sub> nanoplates

Monoclinic and cubic WO<sub>3</sub> nanoplates were prepared from orthorhombic WO<sub>3</sub>·H<sub>2</sub>O nanoplates *via* a facile calcination method at 200 °C for 2 hours, in which WO<sub>3</sub>·H<sub>2</sub>O nanoplates were previously prepared from Na<sub>2</sub>WO<sub>4</sub>·2H<sub>2</sub>O *via* an acid precipitation method. The synthesis procedure is briefly presented in Fig. 1. In detail, a total of 8.25 g of Na<sub>2</sub>WO<sub>4</sub>·2H<sub>2</sub>O (Xilong) was first dissolved in 25 mL of distilled water and stirred for 15 minutes to form a clear Na<sub>2</sub>WO<sub>4</sub> solution. Subsequently, 20 mL of 65% HNO<sub>3</sub> (Merck) was added, followed by gradual addition of distilled water until the total volume of the precursor suspension reached 80 mL. The suspension was continuously stirred for two hours and then transferred to a Teflon container for acid precipitation at RT. After 24 hours, a yellow slurry was obtained, which was thoroughly rinsed several times with distilled water, and then dried in an oven (Nabertherm oven TR120) at 80 °C for 24 h to produce yellow WO<sub>3</sub>·H<sub>2</sub>O aggregates, which were further ground into a powder. The obtained yellow powder was calcined separately in a closed muffle furnace (Nabertherm muffle furnaces L 9/11/B410) and an open tubular furnace (Nabertherm tubular furnace R40/250/12) at 200 °C for 2 hours, yielding white yellow samples, labelled as MF200 and TF200, respectively. The obtained samples were

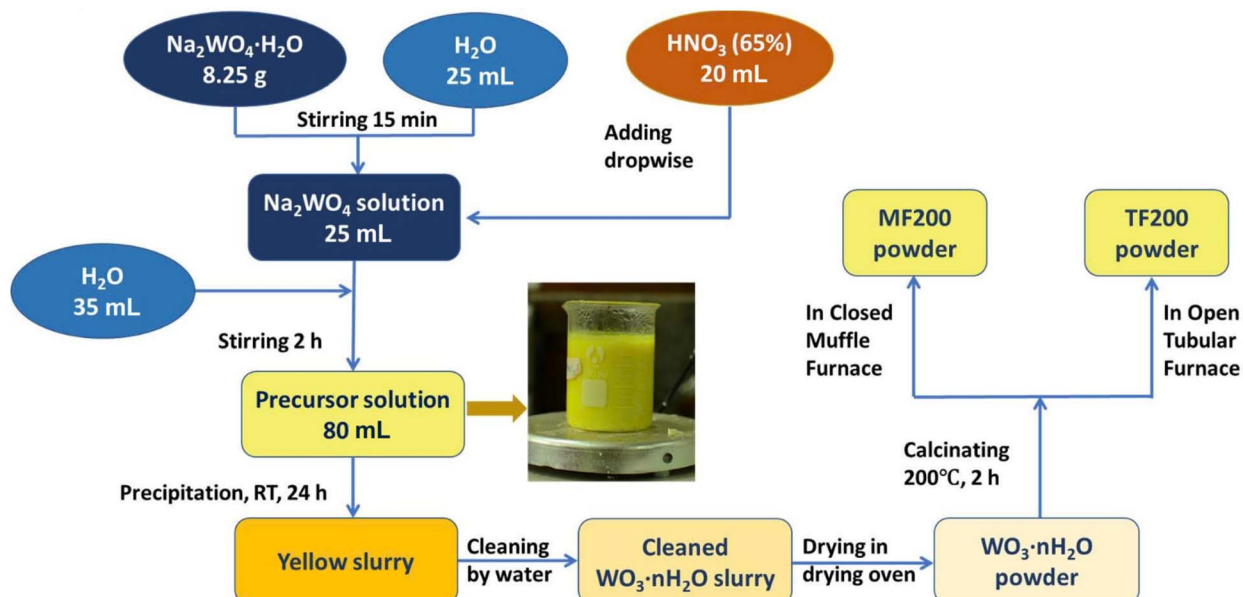


Fig. 1 Schematic of the synthesis process of cubic and monoclinic WO<sub>3</sub> nanostructures.



subsequently utilized for further investigation and evaluation of their gas-sensing performance.

## 2.2. Physicochemical characterizations

The morphological features of the materials were examined using FESEM (Hitachi S4800). The crystal phases of the  $\text{WO}_3$  nanostructures were characterized using X-ray diffraction (XRD) using an X'pert Pro (PANalytical) MPD with  $\text{Cu-K}\alpha$  radiation, employing a scanning rate of  $0.03^\circ$  per 2 s. The specific surface areas of the samples were assessed using Brunauer–Emmett–Teller (BET) method, employing a MicroActive for Tristar II Plus 2.03 system. BET measurements were performed using nitrogen adsorption–desorption isotherms at 77 K, and the samples were degassed at  $200^\circ\text{C}$  under vacuum for 6 h prior to the BET analysis. The optical properties of the samples were investigated by analyzing the diffuse reflectance spectra obtained with a JASCO V-750 diffuse reflectance spectrometer (DRS), operating at a scan speed of  $400 \text{ nm min}^{-1}$ , a bandwidth of 2.0 nm, and a data interval of 0.5 nm.

## 2.3. Fabrication of gas sensors and their gas-sensing measurements

The chemiresistive gas sensors were prepared from calcinated powders *via* drop-coating method. In detail, 20 mg of white yellow  $\text{WO}_3$  powders (TF200 or MF200) was dispersed in 1 mL of dimethylformamide (DMF, Xilong) to obtain a yellow suspension. Subsequently, 0.5  $\mu\text{L}$  of the suspension was drop-coated onto a  $\text{SiO}_2$  substrate with interdigitated Pt electrodes on its surface (Fig. S1†). The substrate was then heated at  $80^\circ\text{C}$  in air for 2 minutes. This step was repeated five times. Finally, the

sensor was calcined at  $200^\circ\text{C}$  for 2 hours to complete the fabrication process.

The gas-sensing performance of the sensors was assessed through a standard automatic measurement system (Fig. S2†). The resistance of the sensors was measured and recorded with a two-point probe, using a high-precision instrument (Keithley 2602A System SourceMeter) connected to a computer. The concentration of the target gas was controlled by adjusting the volumetric ratio of dried air to the test gas in a standard gas chamber *via* a mass flow controller system. The sensing response ( $S$ ) was calculated as  $R_g/R_a$  for oxidizing gases and  $R_a/R_g$  for reducing gases, where  $R_a$  and  $R_g$  represent the resistance of the sensor when exposed to air and the target gas, respectively.

## 3. Results and discussion

### 3.1. Physicochemical properties of the materials

The XRD patterns of the as-synthesized materials are displayed in Fig. 2. The XRD pattern of the as-prepared  $\text{WO}_3$  sample is presented in Fig. 2a, which matches well with the standard ICDD card no. 01-084-0886 of o- $\text{WO}_3$ , with the (111) plane being dominant. The XRD analysis of the MF200 sample (Fig. 2b) confirmed that all the diffraction peaks closely align with the standard ICDD card no. 00-041-0905 for c- $\text{WO}_3$ , exhibiting a lattice constant of  $3.84 \text{ \AA}$ . Specifically, the peaks observed at diffraction angles of  $23.9^\circ$ ,  $33.98^\circ$ ,  $49.25^\circ$ ,  $55.25^\circ$ , and  $61.07^\circ$  correspond to the (100), (110), (111), (200), and (211) crystal planes of c- $\text{WO}_3$ , respectively. All the diffraction peaks of the TF200 sample were consistent with the standard pattern for m- $\text{WO}_3$ , as given in the standard ICDD card no. 01-089-4476. The peaks at  $2\theta$  values of  $23.1^\circ$ ,  $23.7^\circ$ ,  $24.2^\circ$ ,  $34.1^\circ$ ,  $49^\circ$ ,  $56^\circ$ , and  $62^\circ$

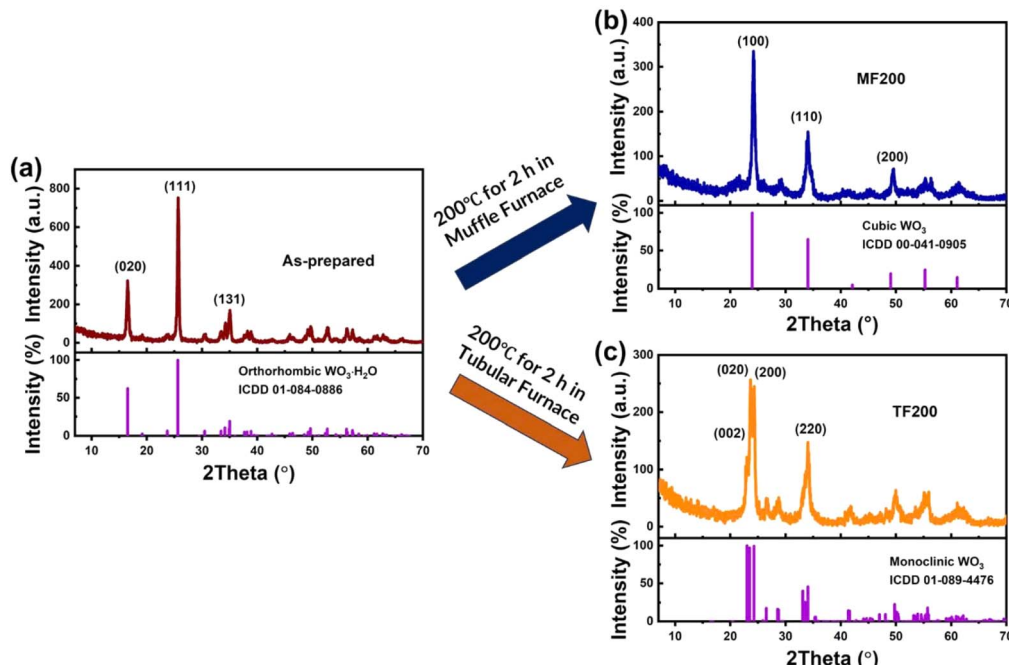


Fig. 2 XRD patterns of the (a) as-prepared  $\text{WO}_3$ , (b) MF200 and (c) TF200 samples in comparison with standard ICDD cards.



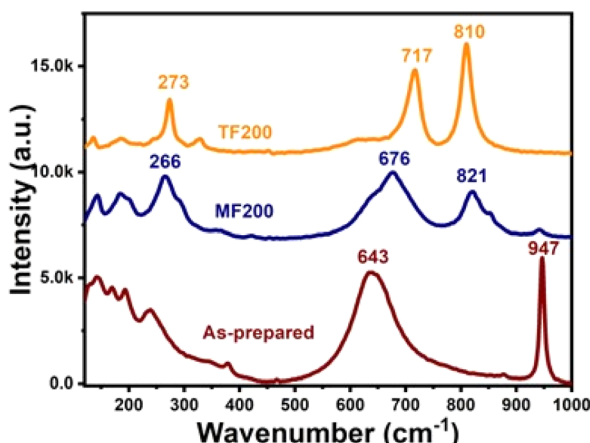


Fig. 3 Raman spectra of the as-prepared  $\text{WO}_3$ , MF200, and TF200 samples.

correspond to the (002), (020), (200), (220), (113), (133), and (202) crystal facets of  $\text{m-WO}_3$ , respectively (Fig. 2c). Furthermore, the absence of any additional diffraction peaks indicated that the synthesized samples possessed high phase purity. These results suggested a complete phase transformation from  $\text{o-WO}_3 \cdot \text{H}_2\text{O}$  to  $\text{m-WO}_3$  and  $\text{c-WO}_3$  through simple calcination in an open tubular furnace and a closed muffle furnace at 200 °C for 2 h, respectively. This difference in phase transformations is attributed to variations in the air environment during calcination, which will be discussed in a later section.

Raman spectroscopy is a valuable technique for analyzing the chemical states and crystal structures at the surface of a material. Fig. 3 shows the Raman spectra of the as-prepared and calcined samples, which further confirm the phase transformation from orthorhombic  $\text{WO}_3 \cdot \text{H}_2\text{O}$  (as-prepared sample) to cubic  $\text{WO}_3$  (MF200) and monoclinic  $\text{WO}_3$  (TF200). In detail, the Raman spectrum of the as-prepared material exhibited two

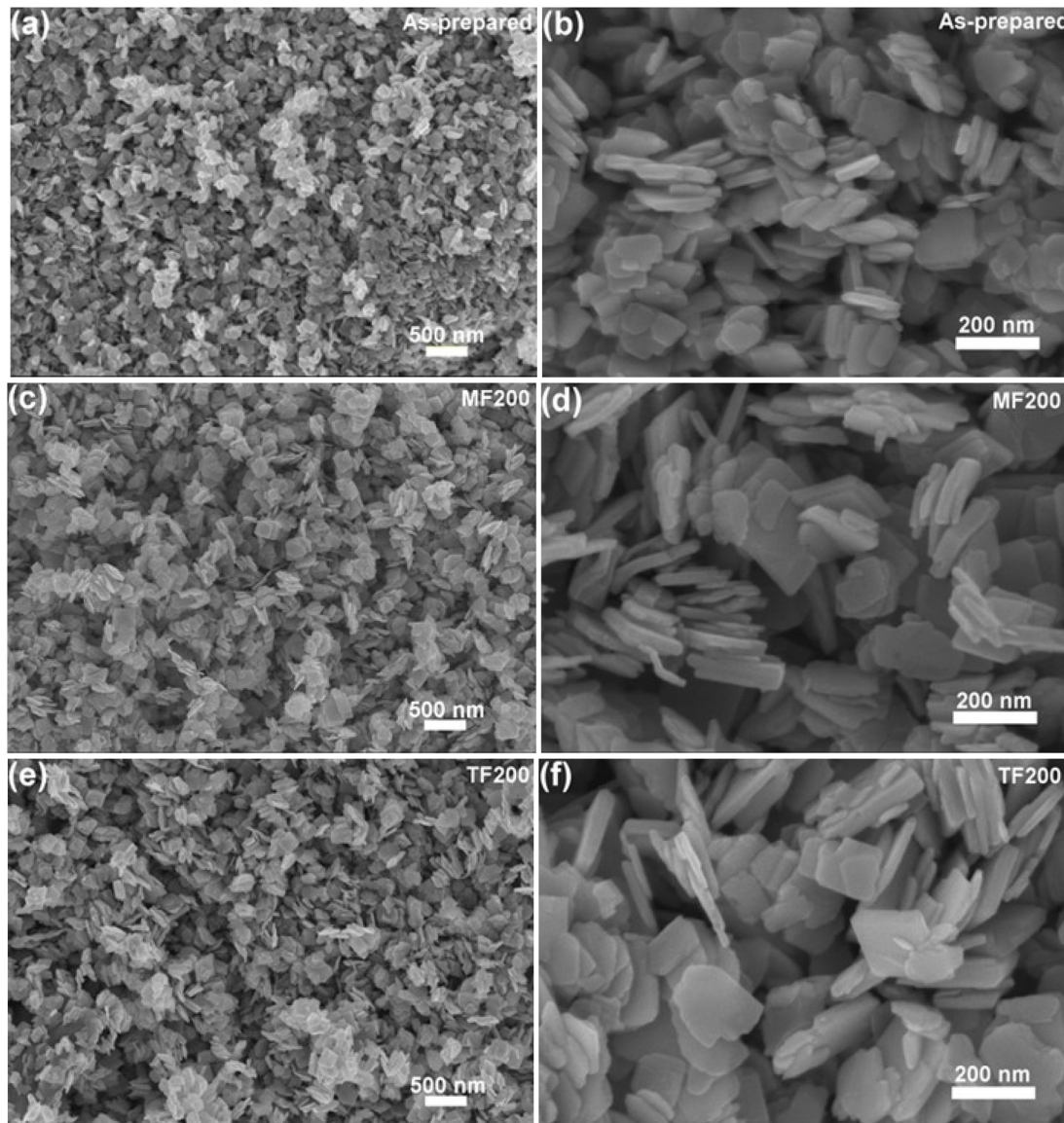


Fig. 4 FESEM images of the as-prepared  $\text{WO}_3$  (a and b), MF200 (c and d) and TF200 (e and f) samples observed at different magnifications.



characteristic peaks at  $643\text{ cm}^{-1}$  and  $947\text{ cm}^{-1}$ , corresponding to the stretching vibrations of the  $\text{O}-\text{W}^{6+}-\text{O}$  and  $\text{W}^{6+}=\text{O}$  bonds in orthorhombic  $\text{WO}_3\cdot\text{H}_2\text{O}$ , respectively.<sup>32-34</sup> In the Raman spectrum of the sample annealed in a muffle furnace, prominent peaks at 266, 676, and  $821\text{ cm}^{-1}$  confirmed the formation of cubic  $\text{WO}_3$ , and these peaks were assigned to the bending  $\delta(\text{O}-\text{W}-\text{O})$  vibration, stretching  $\nu(\text{O}-\text{W}-\text{O})$  vibrations in the equator plane and *via* the axis perpendicular to the equator plane of  $\text{WO}_6$  octahedra of the  $\text{O}-\text{W}-\text{O}$  bonds in cubic  $\text{WO}_3$ , respectively (note that  $\text{WO}_6$  octahedra is the crystal unit in the  $\text{WO}_3$  crystal structure).<sup>35,36</sup> Meanwhile, the Raman spectrum of the sample calcined in a tubular furnace showed distinctive peaks at 273, 717, and  $810\text{ cm}^{-1}$ , corresponding to the bending  $\delta(\text{O}-\text{W}-\text{O})$ , stretching  $\nu(\text{O}-\text{W}-\text{O})$  modes of  $\text{O}-\text{W}-\text{O}$  vibrations in the equator plane and *via* the axis perpendicular to the equator plane of  $\text{WO}_6$  octahedra in monoclinic  $\text{WO}_3$ , respectively, confirming the formation of the monoclinic  $\text{WO}_3$  phase.<sup>33,37-39</sup> Notably, in the Raman spectra of c- $\text{WO}_3$ , a vibration at  $\sim 940\text{ cm}^{-1}$  was clearly observed, implying the vibration of  $\text{W}^{6+}=\text{O}$  bond in the MF200 (c- $\text{WO}_3$ ) sample's surface. Besides, the Raman signals were prominent and distinct, which qualitatively confirmed the high crystallinity of both the as-synthesized and calcined samples.

Fig. 4 presents the FESEM images of the samples measured at different magnifications (20 000 and 100 000 times). Results showed that the as-prepared sample has a nanoplate

morphology (Fig. 4a and b), which is the preferable morphology of orthorhombic  $\text{WO}_3\cdot\text{H}_2\text{O}$  prepared *via* the acid precipitation method in a highly acidic environment.<sup>32</sup> This nanoplate morphology was well preserved after calcination in both the tubular and muffle furnaces, indicating that the calcination process at  $200\text{ }^\circ\text{C}$  induced a minimal effect on the morphology of samples. In the calcined samples, the nanoplates appeared to be more separated (less aggregated) than in the as-prepared sample, and the calcinated nanoplates were thinner. In detail, in the MF200 sample, the nanoplates exhibited different dimensions, but most of these nanoplates exhibited an average size of about  $250\text{ nm} \times 200\text{ nm} \times 40\text{ nm}$  (Fig. 4b and c). In contrast, the TF200 sample contained nanoplates with smooth edges and well-separated structures, with the majority of the larger nanoplates exhibiting an average dimension of  $\sim 200\text{ nm} \times 200\text{ nm} \times 30\text{ nm}$  (Fig. 4e and f).

Surface area plays a crucial role in gas-sensing performance, as a larger surface area generally enhances the sensing capability. BET analysis was carried out to evaluate the surface area, pore diameter, and pore volume of the samples (Fig. 5). Results implied that all the samples exhibited the characteristics of type IV isotherms, with similar pore-size distribution patterns (insets of Fig. 5). Specifically, the specific surface areas of the as-prepared c- $\text{WO}_3$  and m- $\text{WO}_3$  nanomaterials were  $20.8$ ,  $25.0$ , and  $40.6\text{ m}^2\text{ g}^{-1}$ , respectively, with corresponding pore volumes of  $0.136$ ,  $0.146$ , and  $0.178\text{ cm}^3\text{ g}^{-1}$  (Fig. 5a-c and Table 1). These

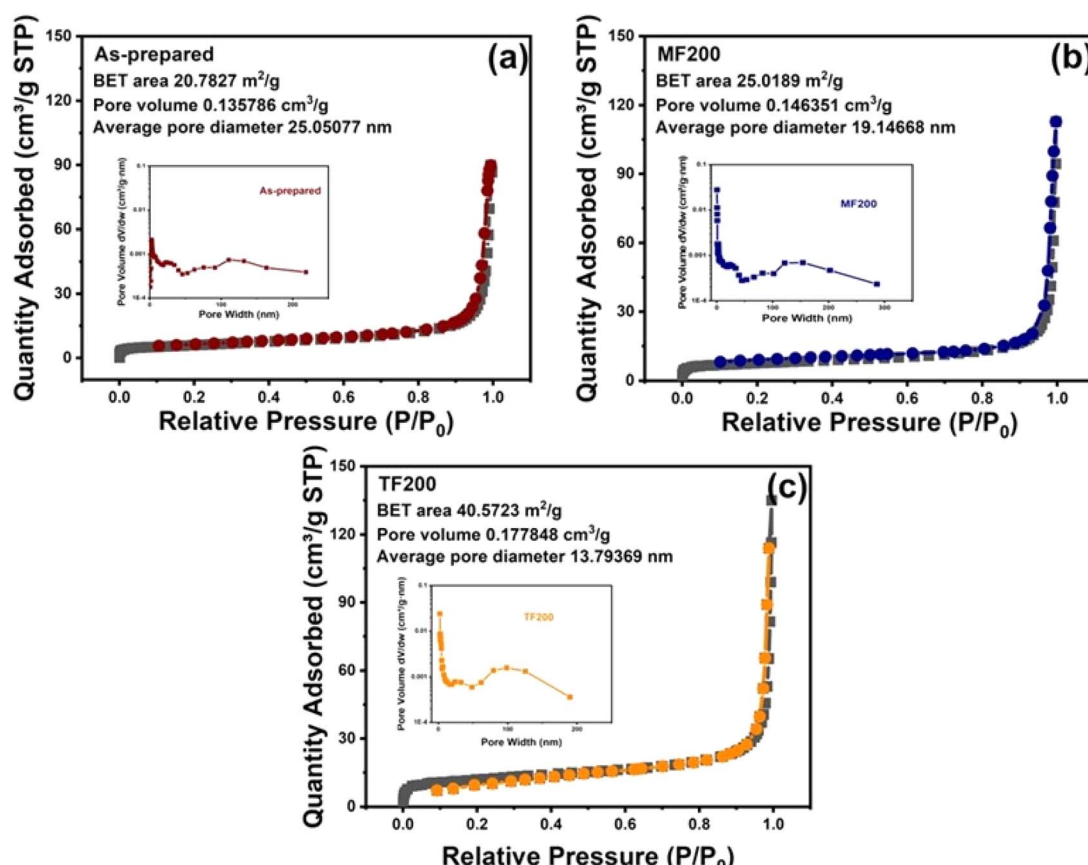


Fig. 5  $\text{N}_2$  adsorption/desorption isotherm and pore size distribution (the inset) of the as-prepared  $\text{WO}_3$  (a), MF200 (b) and TF200 (c) samples.



**Table 1** BET surface area, pore size, and pore volume of the as-prepared and calcined samples

Samples	BET value ( $\text{m}^2 \text{ g}^{-1}$ )	Pore size (nm)	Pore volume ( $\text{cm}^3 \text{ g}^{-1}$ )
As-prepared	20.8	25.0	0.136
MF200	25.0	19.1	0.146
TF200	40.6	13.8	0.178

results suggested that calcination increased the surface area. Furthermore, the m- $\text{WO}_3$  nanomaterials exhibited a larger surface area and pore volume than the c- $\text{WO}_3$  nanomaterials, which were beneficial for enhanced gas adsorption and gas-sensing property.

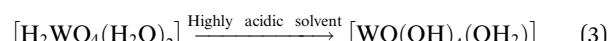
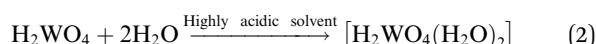
Fig. 6a shows the reflectance spectra of the samples. The as-prepared  $\text{WO}_3$  sample effectively reflected visible light in the 550–900 nm range, while MF200 and TF200 exhibited strong reflection over a wider range of 500–900 nm. These results confirmed the phase transformation from o- $\text{WO}_3$  to c- $\text{WO}_3$  and m- $\text{WO}_3$  after calcination. Further analysis using the derived Kubelka–Munk method estimated the optical bandgaps of the as-prepared  $\text{WO}_3$ , MF200, and TF200 samples to be 2.39 eV, 2.51 eV and 2.69 eV, respectively (Fig. 6b).<sup>38</sup> Furthermore, these results aligned well with the XRD results, where the phase transformation corresponded to the change in optical bandgap.<sup>40</sup>

The formation of orthorhombic  $\text{WO}_3 \cdot \text{H}_2\text{O}$  and the phase transformation from o- $\text{WO}_3 \cdot \text{H}_2\text{O}$  to c- $\text{WO}_3$  and m- $\text{WO}_3$  could be explained by the protonation process occurring during the acid precipitation process<sup>32,34</sup> and the dehydration process occurred during the calcination process, respectively.<sup>34,39</sup> In detail, when  $\text{HNO}_3$  was introduced into the  $\text{Na}_2\text{WO}_4$  solution, neutral tungstic acid ( $\text{H}_2\text{WO}_4$ ) was first produced, as given in eqn (1):

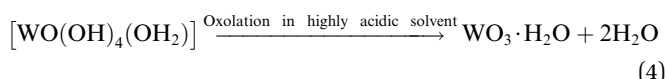


In a highly acidic environment ( $\text{pH} = 1.0$ , measured by Hanna pH meter model HI2020-02), the high concentration of  $\text{H}^+$  promoted the addition of nucleophilic water molecule ( $\text{H}_2\text{O}$ ) to tungstic acid, forming a neutral complex  $[\text{H}_2\text{WO}_4(\text{H}_2\text{O})_2]^0$

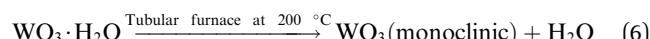
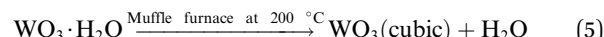
(eqn (2)), which later transformed to a more stable structure of  $[\text{WO}(\text{OH})_4(\text{OH}_2)]^0$  (eqn (3)).<sup>32,34</sup>



After neutral seed molecules  $[\text{WO}(\text{OH})_4(\text{OH}_2)]^0$  were formed, the highly acidic environment further promoted the aggregation of seed molecules through van der Waals forces, leading to the development of a  $\text{WO}_3 \cdot \text{H}_2\text{O}$  crystalline layer. This layer subsequently transformed into  $\text{WO}_3 \cdot \text{H}_2\text{O}$  nanoplates *via* an oxolation process (eqn (4)) during the acid precipitation.



Upon calcination at 200 °C, dehydration was stimulated, which resulted in the phase transition from  $\text{WO}_3 \cdot \text{H}_2\text{O}$  to cubic  $\text{WO}_3$  or monoclinic  $\text{WO}_3$  (eqn (5) and (6), respectively).



In the closed furnace (muffle furnace), dehydration was suppressed owing to the closed ambient, which resulted in the formation of high entropy structure of cubic  $\text{WO}_3$ ; the structure is preferably formed at higher temperatures.<sup>41</sup> Alternatively, in an open-air environment, air (especially oxygen) is continuously supplied, endowing the molecules with more freedom to reorganize, resulting in the formation of the stable monoclinic phase.

### 3.2. Gas-sensing characteristics of the calcined $\text{WO}_3$ nanostructures

The gas-sensing performances were evaluated by monitoring the resistance variation of the sensing material, which

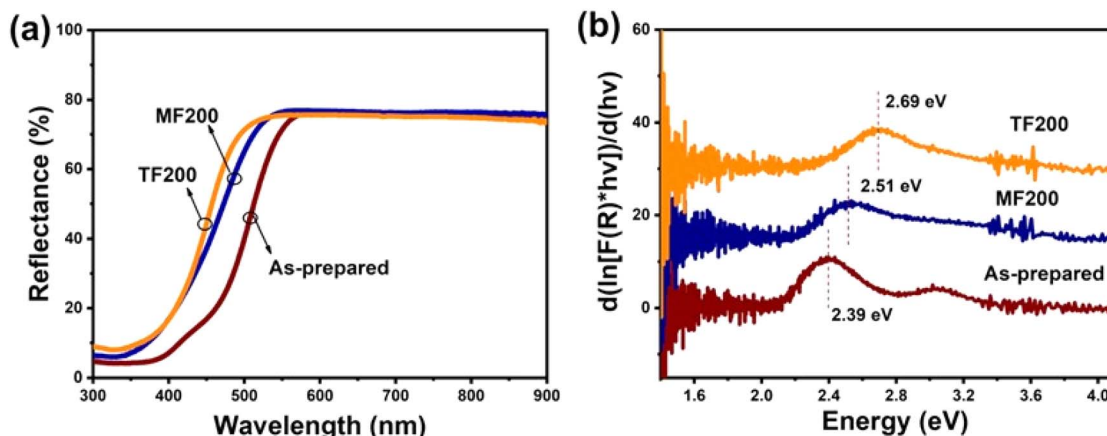


Fig. 6 Comparison of the (a) reflectance spectra and (b) Kubelka–Munk plots of calcined samples with those of the as-prepared sample.



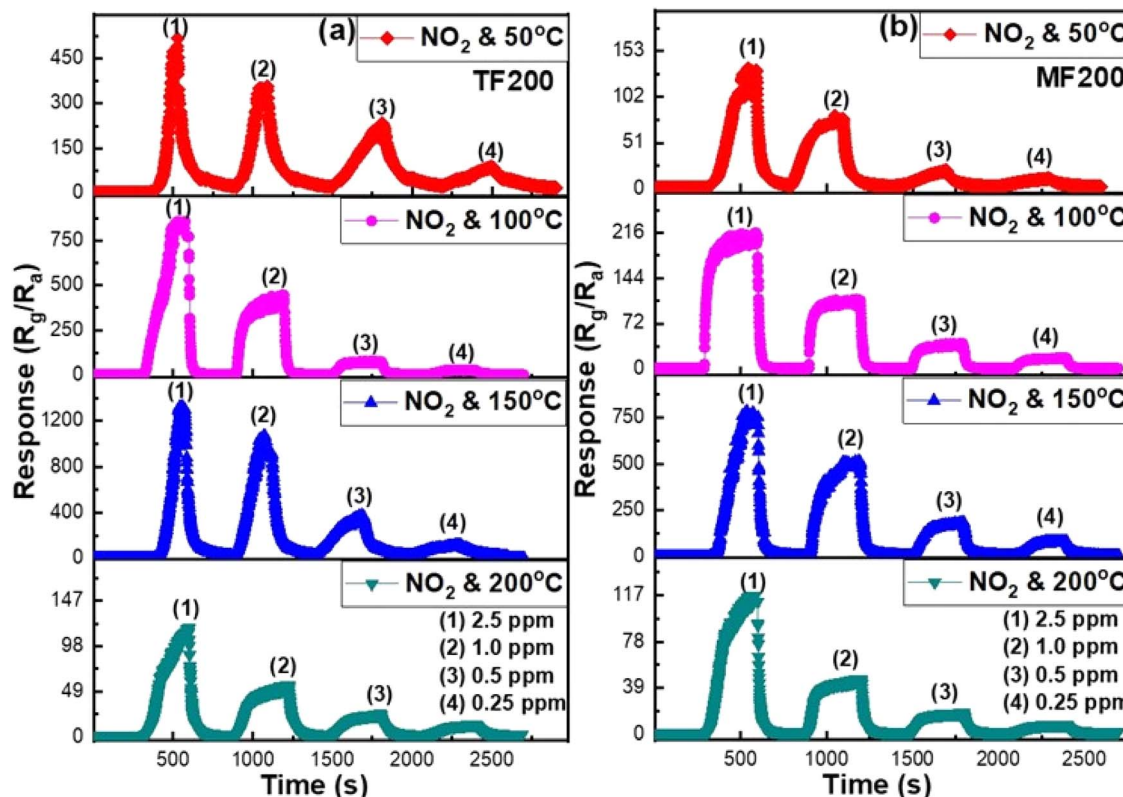


Fig. 7 Gas response changes in the TF200 (a) and MF200 (b) samples towards different concentration of  $\text{NO}_2$  gas at 50–200 °C.

depended on the surrounding gas environment and operating temperature, when exposed to the target gases. The response-time curves of the samples were measured in the concentration range of 0.25–2.5 ppm of  $\text{NO}_2$  at 50–200 °C, as illustrated in Fig. 7 (the corresponding resistance variation with different  $\text{NO}_2$  concentrations at different temperatures are presented in Fig. S3†).

The comparative analysis of the sensing response, response-recovery time, and selectivity between the TF200 and MF200 sensors are indicated in Fig. 8. The effect of temperature on the sensing response was evaluated to identify the optimal working temperature. Fig. 8a presents the sensor response to 2.5 ppm  $\text{NO}_2$  across the temperature range of 50–200 °C. Results indicated that the sensing response of the TF200 and MF200 sensors initially increased as the working temperature increased from 50–150 °C and then declined when the working temperature was increased further to 200 °C. This result implied that 150 °C is the optimal working temperature for both the sensors. Fig. 8b exhibits the sensor response to different  $\text{NO}_2$  concentrations at 150 °C. The TF200 sensor exhibited average response values of 1322, 1061, 366, and 116 for  $\text{NO}_2$  concentrations of 2.5, 1.0, 0.5, and 0.25 ppm, respectively. In contrast, the MF200 sensor showed average response values of 780, 511, 183, and 83 for the same  $\text{NO}_2$  concentrations. These results implied that the TF200 sensor possessed a higher gas response capability than that of the MF200 sensor under same conditions. This phenomenon can be attributed to the large

specific surface area of the TF200 sensor, which increased the number of active sites compared with the MF200 sample.

The effectiveness and reliability of the sensors were also assessed based on their response/recovery time. The values of the TF200 and MF200 sensors for 2.5 ppm  $\text{NO}_2$  at 150 °C are depicted in Fig. 8c. The TF200 sensor exhibited response and recovery times of 239 s and 77 s, whereas the MF200 sensor exhibited response and recovery times of 204 s and 47 s, respectively. Fig. 8d presents the responses of the sensors to 2.5 ppm  $\text{NO}_2$  and 100 ppm of different gases, including  $\text{H}_2$ , ethanol,  $\text{NH}_3$  (reducing gas) and  $\text{H}_2\text{S}$  (oxidizing gas) at 150 °C. Results indicated that the response of the sensors to  $\text{NO}_2$  is obviously greater than their responses to other gases. This was primarily attributed to the unpaired electrons of  $\text{NO}_2$ , making it a highly oxidizing and electronegative gas. Accordingly, when it came into contact with  $\text{WO}_3$ , it readily captured electrons from the surface, leading to a significant increase in the material's resistance. As a result, the sensors demonstrated high selectivity to  $\text{NO}_2$  gas.<sup>42</sup> The selectivity of both m- $\text{WO}_3$  and c- $\text{WO}_3$  to  $\text{NO}_2$  gas can be attributed to the acidic W surface sites generated via the dehydration process, which selectivity adsorbed  $\text{NO}_2$ .<sup>43,44</sup>

In addition, the repeatability of the m- $\text{WO}_3$  and c- $\text{WO}_3$  sensors for 1 ppm  $\text{NO}_2$  at 150 °C is presented in Fig. 9a and b respectively. The dynamic resistance curves exhibited a consistent behaviour across five consecutive test cycles, demonstrating the excellent repeatability of the  $\text{WO}_3$  sensors. This further confirmed their potential as reliable candidates for  $\text{NO}_2$  detection.



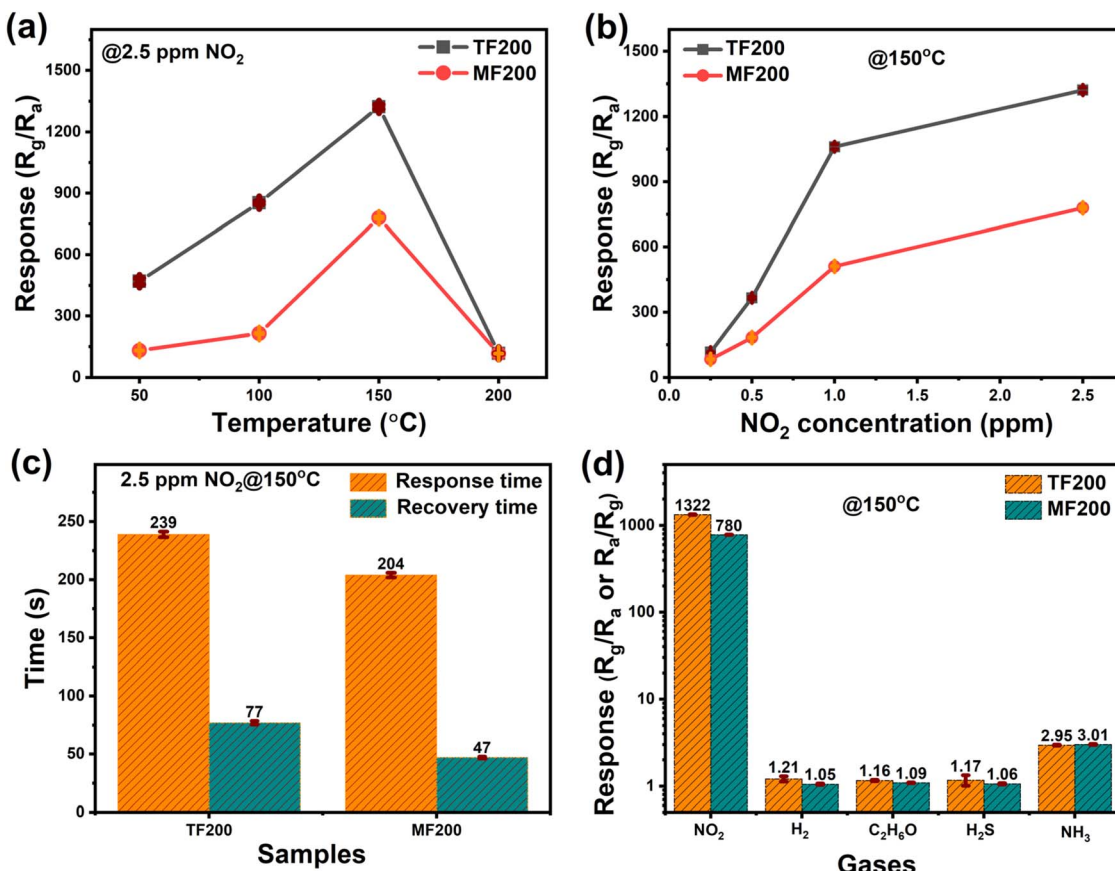


Fig. 8 (a) Response of sensors to 2.5 ppm  $\text{NO}_2$  gas at different temperatures; (b) sensitivity of the sensors to different concentrations of  $\text{NO}_2$  at 150 °C; (c) response and recovery times of the sensors to 2.5 ppm  $\text{NO}_2$  at 150 °C (c); and (d) selectivity of the sensors to 2.5 ppm  $\text{NO}_2$ , 100 ppm ethanol, 100 ppm  $\text{H}_2$ , 100 ppm  $\text{NH}_3$  and 100 ppm  $\text{H}_2\text{S}$  at 150 °C (reported values are average values with standard deviation).

To evaluate the capability of the sensors, we theoretically estimated its limit of detection using the following equation:<sup>45</sup>

$$\text{LoD} = \frac{3(\text{noise}_{\text{rms}})}{\text{slope}} \quad (7)$$

The slope was derived from the first derivative of the linear section of Fig. 9c; noise<sub>rms</sub> was the root mean square (rms) deviation calculated from a polynomial fit of 50 data points collected when exposed to the air (Fig. S4†). The estimated

theoretical detection limits for  $\text{NO}_2$  using the m- $\text{WO}_3$  and c- $\text{WO}_3$  sensors were 0.10 ppb and 0.05 ppb, respectively. These results imply that m- $\text{WO}_3$  and c- $\text{WO}_3$  are highly promising materials as  $\text{NO}_2$  gas sensors, as they are capable of monitoring  $\text{NO}_2$  gas even at sub-ppb level, which is significantly lower than the threshold limit value of 3 ppm established by the American Industrial Hygiene Association.<sup>46</sup>

The  $\text{NO}_2$  gas-sensing mechanism of  $\text{WO}_3$  nanostructure-based sensors can be described as follows: in an air environment, oxygen molecules absorb on the surface layer of  $\text{WO}_3$

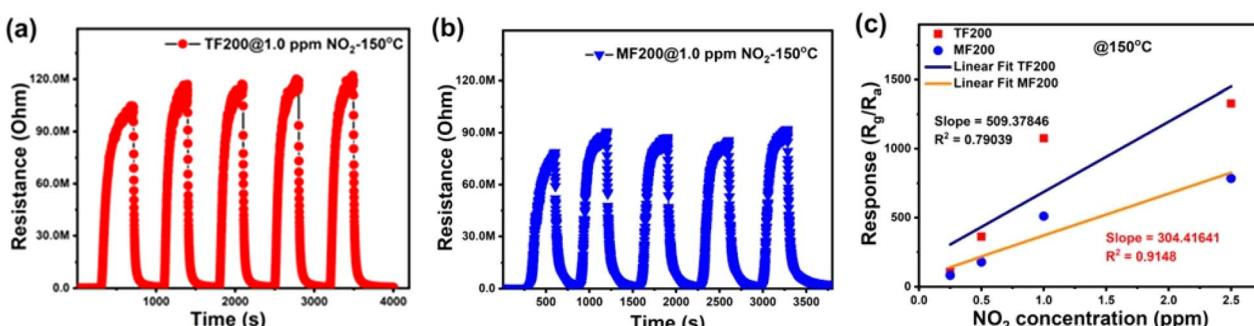
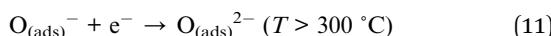
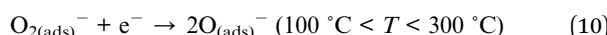
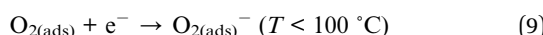


Fig. 9 Repeatability of the TF200 (a) and MF200 (b) sensors to 1 ppm  $\text{NO}_2$  at 150 °C and linear fit curve of the gas response versus gas concentration at 150 °C for the sensors (c).

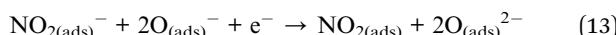
**Table 2** Comparison of NO<sub>2</sub> gas sensing performance of the sensors based on different phases of the WO<sub>3</sub> nanostructure materials reported in recent literature

Materials	Morphology	Working temp. (°C)	NO <sub>2</sub> conc. (ppm)	Response ( $R_g/R_a$ )	$\tau_{res}/\tau_{rec}$ (s)	Ref.
Triclinic	Nanosheets	200	10	228	7/22	25
			5	150	—	
Hexagonal	Nanorods	75	10	5.8	80/100	50
			10	17	50/740	
Orthorhombic	Nanoplates	100	10	60	40/130	51
Monoclinic	Nanoplates	175	5	2.25	12.9/180	52
Hexagonal	Nanoflowers	200	100	1322	239/77	53
Monoclinic	Nanoplates	150	2.5	780	204/47	<b>This work</b>
Cubic						

nanostructure, forming oxygen species (such as O<sub>2</sub><sup>−</sup>, O<sup>−</sup> and O<sup>2−</sup>) at different working temperature.<sup>42</sup> These species capture free electrons from the material's conduction band, leading to charge depletion.



During this process, an electron depletion layer develops on the surface of the WO<sub>3</sub> material, leading to a decrease in the charge carrier concentration and an increase in the resistance. As a strong oxidizing agent, NO<sub>2</sub> not only absorbs on the WO<sub>3</sub> nanostructure's surface but also interacts with the oxygen species, as described by the following equation:<sup>47</sup>



Upon exposure to NO<sub>2</sub> gas, more electrons are extracted from the material, further reducing the charge carrier concentration and widening the electron depletion layer, leading to an increased resistance. Conversely, when NO<sub>2</sub> gas is removed, the electrons previously captured by NO<sub>2</sub> molecules return to the conduction band, shrinking the electron depletion layer and decreasing the resistance.

Notably, c-WO<sub>3</sub> has a narrower optical bandgap and more W<sup>6+</sup>=O bonding on its surface, which theoretically implies better gas-sensing performance than m-WO<sub>3</sub>.<sup>9,44,48</sup> However, the experimental results showed the opposite trend. The better gas-sensing performance of m-WO<sub>3</sub> may be attributed to the dominant contribution of its larger surface area and favorable nanoplate morphology;<sup>46,49</sup> m-WO<sub>3</sub> (TF200) possessed nearly twice the surface area of c-WO<sub>3</sub> (MF200).

Table 2 compares the NO<sub>2</sub> gas-sensing performance of WO<sub>3</sub>-based sensors in different phases.<sup>25,50–53</sup> Among the reported NO<sub>2</sub> gas sensors, those based on m-WO<sub>3</sub> and c-WO<sub>3</sub> exhibited excellent sensitivity at 150 °C, demonstrating high response levels and indicating their potential as candidates for NO<sub>2</sub> gas detection.

## 4. Conclusions

Monoclinic and cubic WO<sub>3</sub> nanoplates were controllably prepared from orthorhombic WO<sub>3</sub>·H<sub>2</sub>O nanoplates *via* a facile calcination process at 200 °C for 2 hours in a tubular furnace and a muffle furnace, respectively. XRD, BET, Raman, and DRS results showed that the calcination process stimulated dehydration in both the furnaces, which resulted in the phase transformation of hydrated WO<sub>3</sub>·H<sub>2</sub>O nanoplates into WO<sub>3</sub> nanoplates. However, different atmospheric environments led to distinct crystal structures. Specifically, under open-air condition (tubular furnace), o-WO<sub>3</sub>·H<sub>2</sub>O was transformed into a stable monoclinic crystal structure, m-WO<sub>3</sub> (TF200), with a surface area of 40.6 m<sup>2</sup> g<sup>−1</sup>. In contrast, under closed-air environment (muffle furnace), o-WO<sub>3</sub>·H<sub>2</sub>O was converted into a high-entropy cubic crystal structure, c-WO<sub>3</sub> (MF200), with a surface area of 25.0 m<sup>2</sup> g<sup>−1</sup>. Notably, both m-WO<sub>3</sub> and c-WO<sub>3</sub> demonstrated excellent gas-sensing characteristics, with ultra-high response, exceptional selectivity, and ultra-low theoretical detection limits, at a mild optimal working temperature of 150 °C. At this temperature, the m-WO<sub>3</sub> and c-WO<sub>3</sub> sensors exhibited average responses of 1322 and 780 to 2.5 ppm NO<sub>2</sub> with theoretical detection limits of 0.10 and 0.05 ppb, respectively. The better NO<sub>2</sub> gas-sensing characteristic of m-WO<sub>3</sub> than that of c-WO<sub>3</sub> was mainly attributed to its larger surface area. This work presents a useful method for the controlled synthesis of WO<sub>3</sub> nanostructures with distinct crystal structures, offering promising potential for various sensing applications.

## Data availability

The data used to support the findings of this study are available from the corresponding author upon reasonable request.

## Author contributions

Dang Trung Do: investigation, methodology, visualization, formal analysis, writing – original draft. Do Y Nhi Nguyen: investigation, formal analysis. Thi Anh Pham: investigation, formal analysis. Cong Tu Nguyen: conceptualization, methodology, formal analysis, writing – review and editing, validation. Van Hieu Nguyen: supervision, validation.



## Conflicts of interest

The authors declare no conflict of interest.

## Acknowledgements

The authors (Do Y Nhi Nguyen and Cong Tu Nguyen) would like to thank the financial support from the Asahi Glass Foundation and Hanoi University of Science and Technology (HUST) through the project number AGF.2024-04.

## References

- 1 S. W. Lee, H. G. Jung, J. W. Jang, D. Park, D. Lee, I. Kim, Y. Kim, D. Y. Cheong, K. S. Hwang, G. Lee and D. S. Yoon, *Sens. Actuators, B*, 2021, **345**, 130361.
- 2 Y. Li, M. Dai, J. Bai, Y. Wang, Y. Li, C. Wang, F. Liu, P. Sun, T. Wang and G. Lu, *Sens. Actuators, B*, 2022, **370**, 132398.
- 3 Y. Ding, B. Du, X. Guo, Y. Dong, M. Zhang, W. Jin, C. Gao, D. Peng and Y. He, *Sens. Actuators, B*, 2024, **414**, 135916.
- 4 M. Jiao, N. Van Duy, D. D. Trung, N. D. Hoa, N. Van Hieu, K. Hjort and H. Nguyen, *J. Electron. Mater.*, 2018, **47**, 785–793.
- 5 K. Iwata, H. Abe, T. Ma, D. Tadaki, A. Hirano-Iwata, Y. Kimura, S. Suda and M. Niwano, *Sens. Actuators, B*, 2022, **361**, 131732.
- 6 S. B. Patil, M. A. More, D. Y. Patil, F. I. Ezema and G. E. Patil, *Mater. Lett.*, 2025, **382**, 137882.
- 7 Q. Wang, R. Li, P. Wang, Y. Zhang, Y. Wang, Y. Yang, Z. Wu, B. An, J. Li and E. Xie, *Sens. Actuators, B*, 2023, **390**, 133985.
- 8 Z. F. Huang, J. Song, L. Pan, X. Zhang, L. Wang and J. J. Zou, *Adv. Mater.*, 2015, **27**, 5309–5327.
- 9 K. K. Devender, B. Palanisamy, A. Jayaram, N. Mani and H. Santhana Krishnan, *ACS Appl. Nano Mater.*, 2024, **8**(1), 65–79.
- 10 R. B. T, P. V. K. Yadav, A. Mondal, K. Ramakrishnan, J. Jarugala, C. Liu and Y. A. K. Reddy, *Chemosphere*, 2024, **353**, 141545.
- 11 Y. Qin, Y. Zhang, J. Lei and S. Lei, *Sens. Actuators, B*, 2025, **428**, 137239.
- 12 L. Jian, R. Peng, Y. He, X. Wang and W. Guo, *Mater. Lett.*, 2023, **336**, 133897.
- 13 L. Pilíai, T. N. Dinhová, M. Janata, D. Balakin, S. Vallejos, J. Otta, J. Štefková, L. Fišer, P. Fitl, M. Novotný, J. Hubálek, M. Vorochta, I. Matolinová and M. Vrňata, *Sens. Actuators, B*, 2023, **397**, 134682.
- 14 M. Wang, Y. Wang, X. Li, C. Ge, S. Hussain, G. Liu and G. Qiao, *Sens. Actuators, B*, 2020, **316**, 128050.
- 15 F. Liu, H. Song, L. Wu, J. Zhao, X. Yao, K. Fu, Z. Jin, J. Liu, F. Wang and Z. Wang, *Colloids Surf. A*, 2023, **666**, 131329.
- 16 D. Kanchan Kumar, P. Bharathi, J. Archana, M. Navaneethan and S. Harish, *Sens. Actuators, B*, 2024, **421**, 136477.
- 17 Z. Wan, C. Ge, L. Bai, S. Hussain, G. Liu, G. Qiao and M. Wang, *Ceram. Int.*, 2024, **50**, 36900–36907.
- 18 H. L. Yu, J. Wang, B. Zheng, B. W. Zhang, L. Q. Liu, Y. W. Zhou, C. Zhang and X. L. Xue, *Sens. Actuators, A*, 2020, **303**, 111865.
- 19 S. Bonam, V. R. Naganaboina, B. Thirupathi and S. G. Singh, *J. Mater. Sci.: Mater. Electron.*, 2024, **35**, 1–12.
- 20 X. Wang, X. Meng and W. Gao, *Sens. Actuators, B*, 2023, **387**, 133790.
- 21 B. An, Y. Yang, J. Yan, Y. Wang, R. Li, Z. Wu, T. Zhang, R. Han, X. Cheng, Q. Wang and E. Xie, *Appl. Surf. Sci.*, 2025, **692**, 162722.
- 22 S. Cao, C. Zhao, T. Han and L. Peng, *Mater. Lett.*, 2016, **169**, 17–20.
- 23 S. Tripathi, D. Tripathi, R. K. Rawat and P. Chauhan, *Mater. Lett.*, 2023, **335**, 133840.
- 24 W. Zeng, B. Miao, T. Li, H. Zhang, S. Hussain, Y. Li and W. Yu, *Thin Solid Films*, 2015, **584**, 294–299.
- 25 L. Han, J. Chen, Y. Zhang, Y. Liu, L. Zhang and S. Cao, *Mater. Lett.*, 2018, **210**, 8–11.
- 26 H. H. Afify, S. A. Hassan, M. Obaida, I. Moussa and A. Abouelsayed, *Opt. Laser Technol.*, 2019, **111**, 604–611.
- 27 S. Wei, J. Zhao, B. Hu, K. Wu, W. Du and M. Zhou, *Ceram. Int.*, 2017, **43**, 2579–2585.
- 28 F. Liu, H. Song, L. Wu, J. Zhao, X. Yao, K. Fu, Z. Jin, J. Liu, F. Wang and Z. Wang, *Colloids Surf. A*, 2023, **666**, 131329.
- 29 Z. Liu, M. Miyauchi, T. Yamazaki and Y. Shen, *Sens. Actuators, B*, 2009, **140**, 514–519.
- 30 Y. Chen, K. Xue and Z. Wang, *Mater. Sci. Semicond. Process.*, 2025, **188**, 109211.
- 31 L. Zhang, F. Li, Y. Yang, D. Li, H. Yu, X. Dong and T. Wang, *Microchem. J.*, 2024, **205**, 111243.
- 32 N. L. Pham, T. L. A. Luu, H. L. Nguyen and C. T. Nguyen, *Mater. Chem. Phys.*, 2021, **272**, 125014.
- 33 M. F. Daniel, B. Desbat, J. C. Lassegues, B. Gerand and M. Figlarz, *J. Solid State Chem.*, 1987, **67**, 235–247.
- 34 N. L. Pham, T. L. A. Luu, T. T. M. Nguyen, V. T. Pham, H. L. Nguyen and C. T. Nguyen, *Commun. Phys.*, 2022, **32**, 307–318.
- 35 G. N. Kustova, Y. A. Chesarov, L. M. Plyasova, I. Y. Lin and A. I. Nizovskii, *Vib. Spectrosc.*, 2011, **55**, 235–240.
- 36 J. De Ribamar Martins Neto, R. M. Torresi and S. I. Cordoba De Torresi, *J. Electroanal. Chem.*, 2016, **765**, 111–117.
- 37 X. V. Le, T. L. A. Luu, H. L. Nguyen and C. T. Nguyen, *Vacuum*, 2019, **168**, 108861.
- 38 C. T. Nguyen, T. P. Pham, T. L. A. Luu, X. S. Nguyen, T. T. Nguyen, H. L. Nguyen and D. C. Nguyen, *Ceram. Int.*, 2020, **46**, 8711–8718.
- 39 V. T. Nguyen, H. S. Nguyen, V. T. Pham, T. T. M. Nguyen, T. L. A. Luu, H. L. Nguyen, D. C. Nguyen and C. T. Nguyen, *Commun. Phys.*, 2020, **30**, 319–330.
- 40 M. J. Priya, P. P. Subha, A. Antony, M. K. Jayaraj and K. Rajeev Kumar, *Chem. Phys. Lett.*, 2023, **829**, 140749.
- 41 N. A. Mohd Razali, W. N. Wan Salleh, F. Aziz, L. W. Jye, N. Yusof and A. F. Ismail, *J. Cleaner Prod.*, 2021, **309**, 127438.
- 42 K. Gu, X. Song, Q. Zhang and M. Zhang, *Sens. Actuators, B*, 2023, **382**, 133453.
- 43 M. Epifani, *Sensors*, 2022, **22**, 2247.
- 44 R. Li, Q. Wang, Y. Wang, B. An, Y. Yang, Z. Wu, P. Wang, T. Zhang, R. Han and E. Xie, *ACS Appl. Mater. Interfaces*, 2024, **16**, 51738–51747.



45 M. J. Priya, C. S. Saramgi, P. P. Subha, A. Antony, M. K. Jayaraj and K. Rajeev Kumar, *Surf. Interfaces*, 2024, **48**, 104340.

46 Y. Li, Q. Zhou, S. Ding and Z. Wu, *Front. Chem.*, 2021, **9**, 1–8.

47 S. S. Sangale, V. V. Jadhav, S. F. Shaikh, P. V. Shinde, B. G. Ghule, S. D. Raut, M. S. Tamboli, A. M. Al-Enizi and R. S. Mane, *Mater. Chem. Phys.*, 2020, **246**, 122799.

48 G.-L. Chen, H.-Y. Jiang, Z.-P. Deng, Y.-M. Xu, L.-H. Huo and S. Gao, *Sens. Actuators, B*, 2024, **415**, 135981.

49 M. Epifani, *Sensors*, 2022, **22**(6), 2247.

50 Y. Shen, H. Bi, T. Li, X. Zhong, X. Chen and A. Fan, *Appl. Surf. Sci.*, 2018, **434**, 922–931.

51 S. S. Shendage, V. L. Patil, S. A. Vanalakar, S. P. Patil, N. S. Harale, J. L. Bhosale, J. H. Kim and P. S. Patil, *Sens. Actuators, B*, 2017, **240**, 426–433.

52 T. Li, Y. Shen, X. Zhong, S. Zhao, G. Li, B. Cui, D. Wei and K. Wei, *J. Alloys Compd.*, 2020, **818**, 152927.

53 G. M. Hingangavkar, Y. H. Navale, T. M. Nimbalkar, R. N. Mulik and V. B. Patil, *Sens. Actuators, B*, 2022, **371**, 132584.

